Divergence-Constrained Physics-Informed Neural Networks for Time-Domain Maxwell's Equations

Chenhong Zhou [1] **Zaifeng Yang** [2] **Xinyu Yang** [2] **Wei Bin Ewe** [2] **Hangwei Qian** [2] **Jie Chen** [1]

[1] *Hong Kong Baptist University, Hong Kong SAR, China* [2]*Institute of High Performance Computing (IHPC), Agency for Science, Technology and Research (A*STAR), Singapore*. Correspondence to: yang_zaifeng@a-star.edu.sg.

1. Introduction

Physics-Informed Neural Networks (PINNs) provide a mesh-free, physics-driven approach for solving partial differential equations by training neural networks to satisfy governing equations and boundary/initial conditions through a composite loss [1, 2, 3]. For electromagnetic modeling, however, PINNs can be challenging in the time domain, especially in resonant settings such as waves confined by perfect electric conductor (PEC) boundaries, where highly oscillatory dynamics and optimization pathologies can lead to degraded accuracy and stability. Time-domain Maxwell's equations are a constrained hyperbolic system: the curl equations drive time evolution while Gauss laws enforce divergence constraints. In FDTD on a Yee lattice, only the curl equations are advanced, yet the staggered-grid discretization and compatible operators help preserve the divergence constraints up to numerical error [4, 5]. In contrast, Maxwell PINNs typically minimize curl-residual losses at collocation points, and they can be curl-consistent yet violate Gauss-law divergence constraints, leading to spurious artifacts, degraded resonant modes, and slower convergence.

Most PINN studies for Maxwell problems focus on the frequency domain [6, 7, 8, 9, 10], with relatively fewer works in the time domain [11, 12, 13, 14]. Across both settings, Gauss-law divergence constraints are often not enforced explicitly, and their impact on time-domain resonant simulations remains underexplored. We address this gap with a divergence-constrained PINN for time-domain Maxwell's equations that augments the curl-residual loss with a divergence regularization term. Experiments on 2D PEC cavity simulation [15] show improved accuracy and convergence for various divergence threshold compared with an unconstrained baseline.

2. Methods

2.1 Time-Domain Governing Equations

The time-domain Maxwell's equations [16] consist of the curl equations, which are formulated as

$$\nabla \times \mathbf{E} = -\mu\, \partial_t \mathbf{H}, \tag{1}$$

$$\nabla \times \mathbf{H} = \epsilon\, \partial_t \mathbf{E} + \mathbf{J}, \tag{2}$$

together with the Gauss-law (divergence) constraints

$$\nabla \cdot (\epsilon \mathbf{E}) = \rho, \tag{3}$$

$$\nabla \cdot (\mu \mathbf{H}) = 0. \tag{4}$$

$\mathbf{E}$ and $\mathbf{H}$ denote the electric and magnetic fields, and ρ and $\mathbf{J}$ denote the electric charge and current densities, respectively. The curl equations (1)–(2) govern the time evolution of the electromagnetic fields, while the divergence equations (3)–(4) impose algebraic constraints that must be satisfied at all times. For source-free regions, where $\rho = 0$ and $\mathbf{J} = \mathbf{0}$, the Gauss-law constraints reduce to homogeneous divergence-free conditions.

2.2 The Proposed Divergence-Constrained PINN

Here, we focus on a two-dimensional transverse-magnetic (TM_z) reduction commonly used in a cavity. Let the spatiotemporal coordinate be $\mathbf{s} = (x, y, t) \in \Omega \times [0, T]$, where $T = dt * nmax$, dt (CFL time step) meets the numerical courant stability condition, and $nmax$ is the total computational timestep.

Given a set of interior collocation points $\{\mathbf{s}_f^{(i)}\}_{i=1}^{N_f}$, we define the Maxwell (curl-form) residual vector as

$$\mathbf{r}_{\mathrm{curl}}(\mathbf{s};\theta) = \begin{bmatrix} r_1(\mathbf{s};\theta) \\ r_2(\mathbf{s};\theta) \\ r_3(\mathbf{s};\theta) \end{bmatrix} = \begin{bmatrix} \mu\, \partial_t H_x(\mathbf{s}) + \partial_y E_z(\mathbf{s}) \\ \mu\, \partial_t H_y(\mathbf{s}) - \partial_x E_z(\mathbf{s}) \\ \epsilon\, \partial_t E_z(\mathbf{s}) - \partial_x H_y(\mathbf{s}) + \partial_y H_x(\mathbf{s}) \end{bmatrix}. \tag{5}$$

where θ denotes trainable parameters in the PINN. The corresponding physics loss due to the curl equations is the mean-squared residual

$$\mathcal{L}_{\mathrm{curl}}(\theta) = \frac{1}{N_f} \sum_{i=1}^{N_f} \left\| \mathbf{r}_{\mathrm{curl}}(\mathbf{s}_f^{(i)};\theta) \right\|_2^2. \tag{6}$$

In this work, we consider a source-free cavity problem with $\rho = 0$ and $\mathbf{J} = \mathbf{0}$, for which the divergence constraints reduce to $\nabla \cdot \mathbf{E} = 0$ and $\nabla \cdot \mathbf{H} = 0$. To mitigate this effect, we explicitly penalize divergence violations by defining the divergence residual

$$r_{\mathrm{div}}(\mathbf{s};\theta) = \nabla \cdot \mathbf{H}(\mathbf{s}) = \partial_x H_x(\mathbf{s}) + \partial_y H_y(\mathbf{s}). \tag{7}$$

We impose this constraint at interior collocation points and optionally also at initial-condition samples, which empirically reduces divergence errors early in training and improves stability over time. The divergence loss over interior points is

$$\mathcal{L}_{\mathrm{div}}^{(f)}(\theta) = \frac{1}{N_f} \sum_{i=1}^{N_f} \left| r_{\mathrm{div}}(\mathbf{s}_f^{(i)};\theta) - \Phi \right|^2, \tag{8}$$

where Φ is the divergence threshold hyperparameter, which is set to 0 by default. The total PINN loss is a combination of the residual loss, initial condition loss, boundary condition loss, and divergence loss.

3. Results and Discussions

Achieving higher precision and faster convergence
We compare the performance of the PINN without

Table 1: Comparison between the PINN without (w/o) and with (w/) the divergence constraint.

RL2E (%)	E_z	H_x	H_y
w/o divergence	5.928	3.420	3.421
w/ divergence	4.188	3.169	3.130
Improvement	29.4%	7.3%	8.5%
MAE (%)	E_z	H_x	H_y
w/o divergence	1.536	0.601	0.600
w/ divergence	1.067	0.569	0.568
Improvement	30.5%	5.3%	5.3%

Table 2: RL2E (%) of the E_z predicted by the PINN without (w/o) and with (w/) the divergence constraint under different timesteps.

nmax	w/o	w/	Improvement
100	3.435	2.246	34.6%
200	3.265	1.684	48.4%
300	4.329	2.874	33.6%
400	5.122	3.899	23.9%
500	5.928	4.188	29.4%
600	9.086	6.656	26.7%
700	48.085	26.120	45.7%

(w/o) and with (w/) the divergence constraint and report the relative L_2 error (RL2E) and mean absolute error (MAE) of the E_z H_x H_y components in Table 1. We observe that the PINN with divergence achieves lower RL2E and MAE for these three components, particularly with significant relative improvements of 29.4% and 30.5% in predicting E_z. In addition, we plot RL2E of the E_z component during training epochs in Fig. 1 to justify that the proposed divergence constraint not only achieves prediction accuracy, but also accelerates training convergence. We visualize the ground truth, prediction errors of the PINN w/o or w/ the divergence constraint in Fig. 2. It can be seen that the constrained model achieves the lower prediction errors, which proves the effectiveness of the proposed divergence constraint.

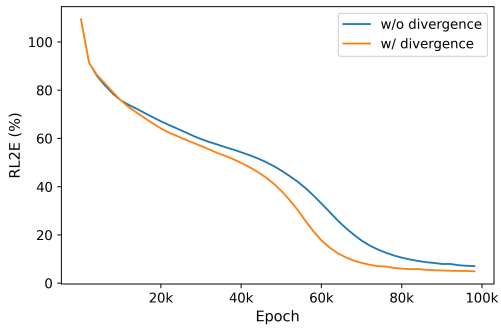

Fig. 1: RL2E of the PINN without (w/o) and with (w/) the divergence constraint during training epochs.

Enabling long-term predictions Table 2 shows the RL2E of the E_z predicted by the PINN without (w/o) and with (w/) the divergence constraint under different timesteps. Despite the increasing prediction difficulty with larger timesteps, the PINN with divergence consistently achieves lower errors. Notably, it brings a 45.7% reduction in error for the long-time domain (700 timesteps), which indicates that our proposed divergence constraint enables the PINN to achieve long-term prediction capability.

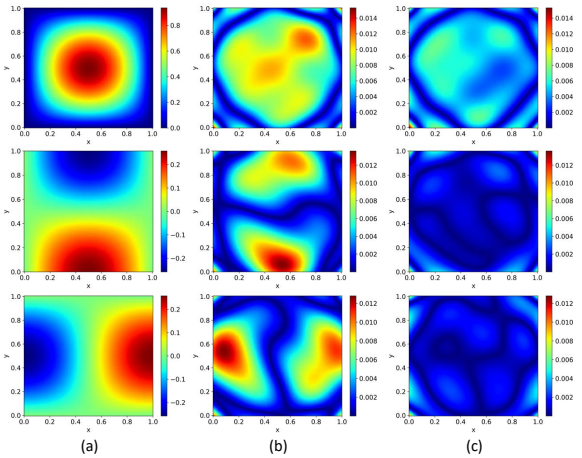

Fig. 2: (a) Ground truth of E_z, H_x, and H_y (from top to bottom) at 200 timesteps; the element-wise absolute prediction error of the PINN without (b) and with (c) the divergence constraint.

The effect of the divergence threshold Fig. 3 shows the results of the constrained PINN with different divergence thresholds Φ. The lowest error occurs at $\Phi = 1e^{-4}$. This indicates that a strict divergence constraint (i.e., 0 or $1e^{-8}$) does not necessarily yield optimal performance, and a slight relaxation of the constraint probably achieves the best results.

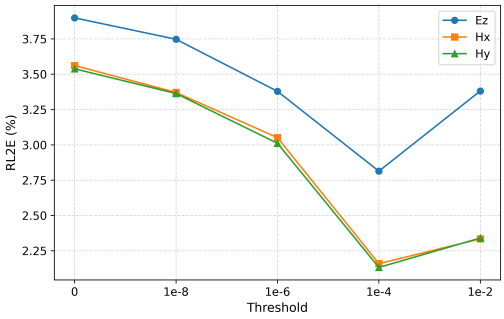

Fig. 3: RL2E of the PINN with the divergence constraint under different thresholds.

4. Conclusion

We introduced a divergence-constrained PINN for time-domain Maxwell's equations by adding a Gauss-law divergence penalty to the curl-residual loss. In 2D PEC cavity tests, this constraint reduced spurious artifacts and improved both accuracy and convergence versus an unconstrained PINN, especially for long-time predictions. The method is simple to implement and extends naturally to 3D Maxwell and other divergence-constrained equations.

Acknowledgments

This work was supported by the Physics Foundation Model initiative at the Institute of High Performance Computing (IHPC), Agency for Science, Technology and Researdh (A*STAR), Singapore.

References

[1] Maziar Raissi, Paris Perdikaris, and George E Karniadakis. Physics-informed neural networks: A deep learning framework for solving forward and inverse problems involving nonlinear partial differential equations. *Journal of Computational Physics*, 378:686–707, 2019.

[2] Maziar Raissi, Paris Perdikaris, and George Em Karniadakis. Physics informed deep learning (part i): Data-driven solutions of nonlinear partial differential equations. *arXiv preprint arXiv:1711.10561*, 2017.

[3] George Em Karniadakis, Ioannis G Kevrekidis, Lu Lu, Paris Perdikaris, Sifan Wang, and Liu Yang. Physics-informed machine learning. *Nature Reviews Physics*, 3(6):422–440, 2021.

[4] Allen Taflove, Susan C Hagness, and Melinda Piket-May. Computational electromagnetics: the finite-difference time-domain method. *The Electrical Engineering Handbook*, 3(629-670):15, 2005.

[5] Dennis M Sullivan. *Electromagnetic simulation using the FDTD method*. John Wiley & Sons, 2013.

[6] Lu Lu, Xuhui Meng, Zhiping Mao, and George Em Karniadakis. Deepxde: A deep learning library for solving differential equations. *SIAM review*, 63(1):208–228, 2021.

[7] Levi D McClenny and Ulisses M Braga-Neto. Self-adaptive physics-informed neural networks. *Journal of Computational Physics*, 474:111722, 2023.

[8] Bochen Wang, Zhenwei Guo, Jianxin Liu, Yanyi Wang, and Fansheng Xiong. Geophysical frequency domain electromagnetic field simulation using physics-informed neural network. *Mathematics*, 12(23):3873, 2024.

[9] Sifan Wang, Yujun Teng, and Paris Perdikaris. Understanding and mitigating gradient flow pathologies in physics-informed neural networks. *SIAM Journal on Scientific Computing*, 43(5):A3055–A3081, 2021.

[10] Chao Song, Tariq Alkhalifah, and Umair Bin Waheed. A versatile framework to solve the helmholtz equation using physics-informed neural networks. *Geophysical Journal International*, 228(3):1750–1762, 2022.

[11] Maryam Nihad Salem, Nebras Jalel Ibrahim, Walaa Badr Khudhair, Hassan Al-Mahdawi, Zainab Hassan Mohammed, Zainab khazal Shamel, and Alaulddin Mueen Latfa. Physics-informed neural networks for solving maxwell's equations in electromagnetic wave propagation. *Academia Open*, 10(2):10–21070, 2025.

[12] Alexandre Pugin, Stéphane Lanteri, Stéphane Descombes, and Mahmoud Elsawy. *Application of Physics-Informed Neural Networks to Maxwell equations*. PhD thesis, Centre Inria d'Université Côte d'Azur, 2025.

[13] Xiang Huang, Hongsheng Liu, Beiji Shi, Zidong Wang, Kang Yang, Yang Li, Min Wang, Haotian Chu, Jing Zhou, Fan Yu, et al. A universal pinns method for solving partial differential equations with a point source. In *IJCAI*, pages 3839–3846, 2022.

[14] Gal G Shaviner, Hemanth Chandravamsi, Shimon Pisnoy, Ziv Chen, and Steven H Frankel. Pinns for solving unsteady maxwell's equations: convergence issues and comparative assessment with compact schemes. *Neural Computing and Applications*, 37(29):24103–24122, 2025.

[15] David M Pozar. *Microwave engineering: theory and techniques*. John wiley & sons, 2021.

[16] Constantine A Balanis. *Advanced engineering electromagnetics*. John Wiley & Sons, 2012.

Appendix A. 2D PEC Cavity Electromagnetic Problem (TM_z)

1.1 Geometry and material model

We consider a two-dimensional rectangular perfectly electric conductor (PEC) cavity

$$\Omega = [0, L_x] \times [0, L_y], \tag{A1}$$

filled with a homogeneous, isotropic medium with constant permittivity ϵ and permeability μ. Unless otherwise stated, we use a dimensionless (natural-unit) setting with $\epsilon = \mu = 1$, so that the wave speed is $c = 1/\sqrt{\epsilon\mu} = 1$.

1.2 TM_z polarization and reduced Maxwell equations

Under the transverse-magnetic (TM_z) assumption, the nonzero field components are

$$\mathbf{E}(x, y, t) = (0, 0, E_z(x, y, t)), \tag{A2}$$

$$\mathbf{H}(x, y, t) = (H_x(x, y, t), H_y(x, y, t), 0). \tag{A3}$$

For a source-free cavity ($\rho = 0$ and $\mathbf{J} = \mathbf{0}$), the time-domain Maxwell curl equations reduce to

$$\mu\, \partial_t H_x + \partial_y E_z = 0, \tag{A4}$$

$$\mu\, \partial_t H_y - \partial_x E_z = 0, \tag{A5}$$

$$\epsilon\, \partial_t E_z - \partial_x H_y + \partial_y H_x = 0. \tag{A6}$$

A Gauss-law (divergence) constraint associated with the magnetic field is

$$\nabla \cdot \mathbf{H} = \partial_x H_x + \partial_y H_y = 0, \tag{A7}$$

which corresponds to $\nabla \cdot \mathbf{B} = 0$ when $\mathbf{B} = \mu \mathbf{H}$ and μ is constant.

Eliminating $\mathbf{H}$ from (A4)–(A6) yields a scalar wave equation for E_z:

$$\partial_{tt} E_z = c^2 \left(\partial_{xx} E_z + \partial_{yy} E_z \right), \qquad c = \frac{1}{\sqrt{\epsilon \mu}}. \tag{A8}$$

1.3 Boundary conditions (PEC cavity)

On a PEC boundary, the tangential electric field vanishes:

$$\mathbf{n} \times \mathbf{E} = \mathbf{0} \quad \text{on } \partial\Omega, \tag{A9}$$

where $\mathbf{n}$ is the outward unit normal. For TM_z polarization in 2D, this reduces to the Dirichlet condition

$$E_z(x, y, t) = 0, \qquad (x, y) \in \partial\Omega, \ t \in [0, T]. \tag{A10}$$

1.4 Initial condition

To excite a cavity eigenmode, we use a standing-wave initial condition consistent with (A10). A convenient consistent initialization is therefore

$$E_z(x, y, 0) = E_0 \sin(k_x x) \sin(k_y y), \tag{A11}$$
$$H_x(x, y, 0) = 0, \tag{A12}$$
$$H_y(x, y, 0) = 0, \tag{A13}$$

corresponding to a purely standing-wave electric field at $t = 0$, where k_x and k_y are the wave numbers along x and y directions.

Appendix B. Convergence Contributing to Long-Time Simulation Capability

We plot the RL2E curve of the PINN without (w/o) and with (w/) the divergence constraint under different timesteps in Fig. A1. It is consistent with the conclusion obtained from the Table 2, justifying the advantage of the proposed constraint that empowers the PINN with longer prediction capability.

Appendix C. More Visualization Results

We provided more visualization results in Fig. A2 and Fig. A3, which shows the results at the initial time and the 100 timesteps, respectively. It can be seen that the constrained PINN consistently achieves the lower prediction errors, demonstrating the effectiveness of the proposed constraint.

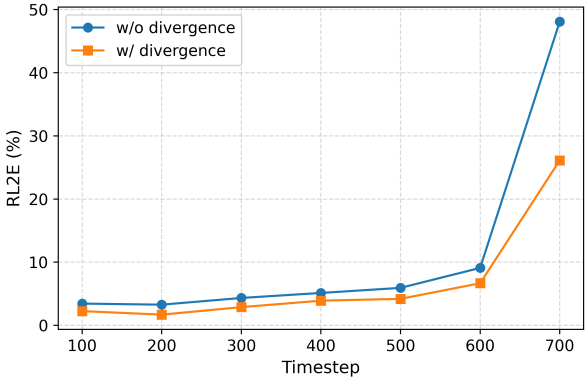

Fig. A1: RL2E of the PINN without (w/o) and with (w/) the divergence constraint under different timesteps.

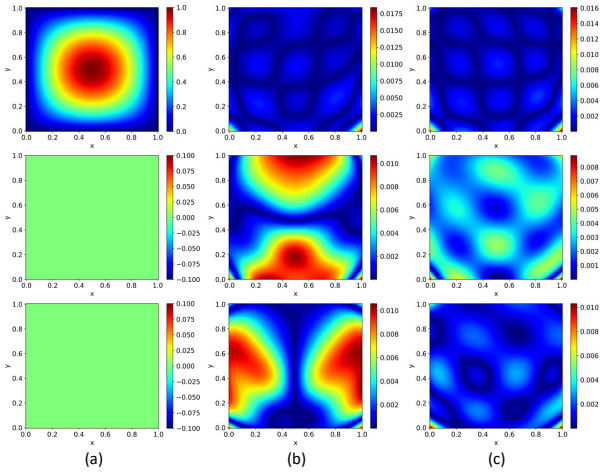

Fig. A2: (a) Ground truth of E_z, H_x, and H_y (from top to bottom) at the initial time; the element-wise absolute prediction error of the PINN without (b) and with (c) the divergence constraint.

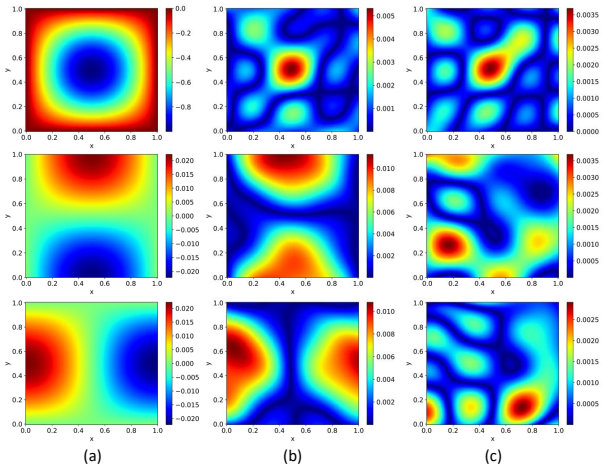

Fig. A3: (a) Ground truth of E_z, H_x, and H_y (from top to bottom) at 100 timesteps; the element-wise absolute prediction error of the PINN without (b) and with (c) the divergence constraint.